Deep–Sea Research II 177 (2020) 104742

Contents lists available at ScienceDirect

Deep-Sea Research Part II

journal homepage: http://www.elsevier.com/locate/dsr2

# Stratification, plankton layers, and mixing measured by airborne lidar in the Chukchi and Beaufort seas

James H. Churnside [a,*], Richard D. Marchbanks [b], Svein Vagle [c], Shaun W. Bell [d], Phyllis J. Stabeno [e]

[a] NOAA Earth System Research Laboratory, Boulder, CO, USA
[b] Cooperative Institute for Research in the Environmental Sciences, University of Colorado and NOAA Earth System Research Laboratory, Boulder, CO, USA
[c] Institute of Ocean Sciences, Fisheries and Oceans Canada, Sidney, British Columbia, Canada
[d] Joint Institute for the Study of the Atmosphere and Oceans, University of Washington and NOAA Pacific Marine Environmental Laboratory, Seattle, WA, USA
[e] NOAA Pacific Marine Environmental Laboratory, Seattle, WA, USA

ARTICLE INFO

*Keywords:*
Ocean lidar
Arctic ocean
Subsurface plankton layers
Ocean optics
Barrow canyon
Turbulence
Ocean remote sensing

ABSTRACT

A total of 4.9 million vertical profiles of optical backscattering were measured by airborne lidar in July of 2014 and July of 2017 in the Chukchi and Beaufort seas. We found very different ice conditions in the study area between July 2014 and July 2017, but the characteristics of subsurface plankton layers measured by the lidar and their dependence on ice cover were similar for the two years. In both years, the prevalence of subsurface plankton layers exponentially decreased with increasing ice cover. The average depths were similar for both years, with layers in open water deeper than those in the pack ice. The depths of subsurface plankton layers were consistent with mixed layer depth in areas where *in situ* density profiles were available. A noticeable difference in layer strength (defined as the ratio of the layer signal to the background) was likely caused by higher background phytoplankton concentrations in 2017. Differences in layer thickness were observed, which could be the result of higher current shears in 2017. Turbulent mixing of phytoplankton and zooplankton in Barrow Canyon was inferred from the power spectral density of lidar and acoustic scattering. Lidar measurements suggested that the level of turbulence and its vertical distribution were affected by local upwelling-favorable winds. The vertical distribution of acoustic scattering was different from that of the lidar, which we interpret as different vertical distributions of phytoplankton and zooplankton.

## 1. Introduction

The climate of the Arctic is rapidly changing as a result of several amplifying feedback mechanisms (Pithan and Mauritsen, 2014; Serreze and Barry, 2011; Taylor et al., 2013). These include decreases in surface albedo, increases in cloud cover, and increased atmospheric transport from the south. The largest factor in determining surface albedo is sea ice, which has been shrinking in extent, becoming thinner, and drifting more rapidly (Comiso, 2011; Kwok and Rothrock, 2009; Spreen et al., 2011; Vaughan et al., 2013). In turn, the reduction in sea ice affects the timing and distribution of phytoplankton blooms. Satellite observations suggest that the primary productivity of the Arctic Ocean is increasing as the area of open water and the length of growing season increase (Arrigo and van Dijken, 2015; Arrigo et al., 2008). In addition, thinning ice and more melt ponds allow increased primary productivity under the ice (Arrigo et al., 2014).

Sub-surface phytoplankton layers are common in the Arctic Ocean in summer (Ardyna et al., 2013; Cota et al., 1996; Coupel et al., 2011). As nutrients are depleted at the surface, a plankton layer develops at the pycnocline formed by melting ice (Brown et al., 2015; Hill and Cota, 2005; Martin et al., 2010; Naoya et al., 2018). While the depth of these layers is generally consistent with measured pycnocline depths, some can be much deeper. Brown reported depths ranging from 3 to 106 m, but with a mode of 15–20 m in July. This is consistent with a previous suggestion that there might be shallow layers associated with the pycnocline, but also deep layers that might be associated with the deeper nutricline (Churnside and Marchbanks, 2015; Martin et al., 2013). While this work is all in the Arctic Ocean, we should note that thin plankton layers associated with a salinity-driven pycnocline have also been observed in Magellan Strait in the Southern Ocean (Ríos et al., 2016).

* Corresponding author.
*E-mail address:* james.h.churnside@noaa.gov (J.H. Churnside).

https://doi.org/10.1016/j.dsr2.2020.104742
Received 29 May 2019; Received in revised form 25 January 2020; Accepted 26 January 2020
Available online 31 January 2020

Subsurface plankton layers affect primary productivity. In the northern Barents Sea, productivity in the subsurface plankton layer was measured to be similar to that during the spring bloom (Hegseth, 1998). In the central North Sea, 58% of the total column productivity in August was in a subsurface plankton layer, and 37% of the annual average was in this layer (Weston et al., 2005, 2011). Measurements in the Beaufort Sea found 55% of the productivity in the subsurface layer (Retamal et al., 2008), and models suggest that 35–90% of the coastal productivity in the Beaufort Sea is within the subsurface layer (Martin et al., 2013). A comparison of 32 models found that the models generally performed better in regions where there was no subsurface layer (Lee et al., 2015). It has been noted that models often overestimate primary production, and this can compensate for not including production of the subsurface layer, resulting in an overall estimate that might be better than expected (Arrigo et al., 2011; Lee et al., 2015). In fact, column integrated productivity can be negatively correlated with surface chlorophyll, because low surface chlorophyll is often associated with a subsurface chlorophyll layer with high productivity (Jacox et al., 2015).

Within the Arctic Ocean, Barrow Canyon is a region that has received a lot of attention. Much of the water flowing northward through the Bering Strait passes through the canyon, especially in summer. Summertime estimates range from 50% (Stabeno et al., 2018) to 80% (Gong and Pickart, 2015), and an annual average of 55% has been reported (Itoh et al., 2013). Together with this influx of water from the south, Barrow Canyon is also biologically active and has been designated as one of eight regions of the Distributed Biological Observatory, which was implemented to monitor changes in the Arctic Ocean (Grebmeier et al., 2010; Moore and Grebmeier, 2018). Flow through the canyon might also be expected to generate turbulent mixing, and a direct measurement of turbulent kinetic energy dissipation near the head of the canyon along the 70-m isobath on the northern side showed elevated levels near the pycnocline and also within the boundary layer near the bottom (Shroyer et al., 2014).

There have been a number of investigations of plankton using lidar (Churnside, 2014; Churnside and Ostrovsky, 2005; Churnside and Donaghay, 2009; Churnside et al., 2012), but few in the Arctic. Hill and Zimmerman (2010) used model results to show that primary production estimates in the Arctic could be improved with lidar. Goldin et al. (2007) used an airborne lidar to detect subsurface layers in the Barents Sea in August of 2003. We used a similar lidar to provide more details of the structure of subsurface layers in the Chukchi and Beaufort seas in 2014 (Churnside and Marchbanks, 2015). Beherenfeld et al. (2017) estimated phytoplankton biomass in the Arctic using the depth-integrated return from a space-based lidar that lacks depth resolution required for profiling. That same lidar has been used to detect sea ice (Lu et al., 2017). We should note that lidar provides vertical profiles of phytoplankton backscattering, while many of the plankton layer studies listed above were based on chlorophyll measurements, (e.g. Arrigo et al., 2011; Hill et al., 2005; Weston et al., 2005) The depth distributions of the two quantities can be different because of photo-acclimation by phytoplankton (Kitchen and Zaneveld, 1990).

In this paper, we report the results of lidar surveys in 2017 and compare these with our 2014 results. These results are based on 4.9 million lidar profiles of optical backscattering in the ocean. The survey periods were the same for the two years, but the ice conditions were very different. Because these measurements were only three years apart, the differences were well within the range of natural variability. However, to the extent that the results depend on ice cover, they can be used to predict the characteristics of subsurface plankton layers in July as Arctic sea ice continues to retreat.

## 2. Materials and methods

The study area and period (15–31 July) of investigation were the same as in 2014, except that the flight locations were adjusted in response to the different ice conditions. Fig. 1 shows the flight tracks for the two years, along with the ice extent at the beginning (July 15) and end (July 31) of the study. Only airborne lidar is capable of measuring subsurface plankton layers over this geographical extent within a two-week period. In both years, the objective of each flight was to fly from open water to full ice cover or the reverse along as many lines as possible consistent with weather conditions. The platform was a National Oceanographic and Atmospheric Administration (NOAA) Twin Otter flying at 300 m altitude at a speed of about 60 m $s^{-1}$. Ice-extent values are from satellite-derived maps of the marginal ice zone from the US National Ice Center. These are provided for context, and were not used in the analysis. Additionally, daily ice-extent values were obtained from the National Snow and Ice Data Center (Fetterer et al., 2010) and averaged over the period July 15–31 for each year.

The primary instrument for this investigation, as in 2014, was the NOAA airborne oceanographic lidar (Fig. 2). This lidar transmitted 12 ns pulses of linearly polarized green (532 nm) light at a rate of 30 Hz. Two receiver channels detected the co- and cross-polarized light scattered from the ocean with a 1 GHz sample rate. Processing of the lidar data to obtain layer parameters has been described in detail in (Churnside and Marchbanks, 2017). Briefly, the technique assumes that, for every lidar return, the lidar attenuation and scattering parameters can be expressed as the sum of a component that is constant with depth and a perturbation that is depth dependent (Churnside and Marchbanks, 2017). A linear regression of the logarithm of the return with depth is used to find the constant components. We then assume that the integral of the attenuation coefficient perturbation from the surface to each depth is small, although the perturbation itself at any depth need not be. Layers were identified visually from plots of the scattering perturbation parameter with depth. For each identified layer, the averages of the depth of the maximum of the scattering perturbation (layer depth), the full width at half maximum of the perturbation peak (layer thickness), and the value of the maximum divided by the constant return (layer strength) were calculated. Fractional ice cover was also obtained from the lidar, based on the fraction of pulses in each kilometer of flight track where the surface return saturated the detector.

To investigate turbulent mixing in Barrow Canyon, five transects of the canyon were selected (Fig. 3). Bathymetric data were obtained from the International Bathymetric Chart of the Arctic Ocean (IBCAO) Version 3.0 (Jakobsson et al., 2012), and the flight segment where the depth is greater than 70 m was used to define the canyon. Within the inertial subrange of spatial wavelengths, the power-spectral density (*psd*) of a passive scalar sampled along a line through a turbulent field is given by (Sreenivasan, 1996)

$$psd = TK^{-5/3}, \tag{1}$$

where $T$ is a measure of turbulence strength that depends on the units of the measured quantity and $K$ is the spatial wavelength. In our case, we calculated the *psd* of data series constructed by taking a single sample of the lidar return at the same depth from each pulse across the canyon. To investigate depth differences, depths of 10 and 20 m were used for each transect. To obtain large spatial scales, we used the full length of each transect, so no information about the distribution of mixing along transects is possible. A linear regression of the logarithm of the *psd* to the logarithm of spatial wavelength was calculated for each transect at each of the two depths.

Water density profiles were measured at 71.219°N, 164.257°W using the NOAA Prawler (PRofiling crAWLER) (Osse et al., 2015; Tabisola et al., 2017). This instrument provided CTD (Conductivity Temperature Depth) profiles at 3 h intervals beginning July 29, 2017, and data through August 5, 2017 were considered in the analysis. For each profile, potential density was calculated from temperature and salinity, and the depth where the derivative of potential density with depth was maximum (maximum Brunt-Väisälä frequency) was used as a measure of the mixed layer depth (Bourgain and Gascard, 2011). Each profile of potential density was plotted and inspected to ensure that the measured

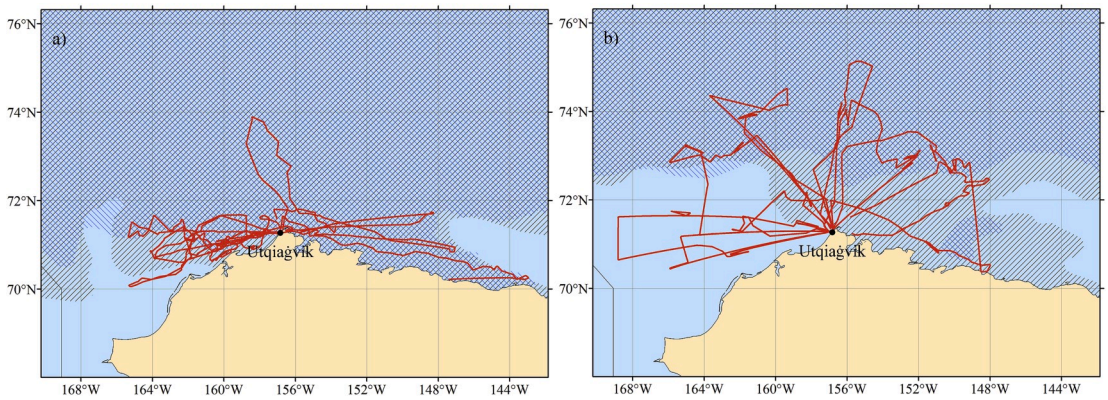


**Fig. 1.** Map of study area near northern Alaska in **a)** July 2014 and **b)** July 2017. Black///denotes the area covered by ice on July 15, and blue \\ denotes the area covered by ice on July 31 of each year. Red lines are the aircraft flight tracks, and the black circle marks the airport in Utqiaġvik.

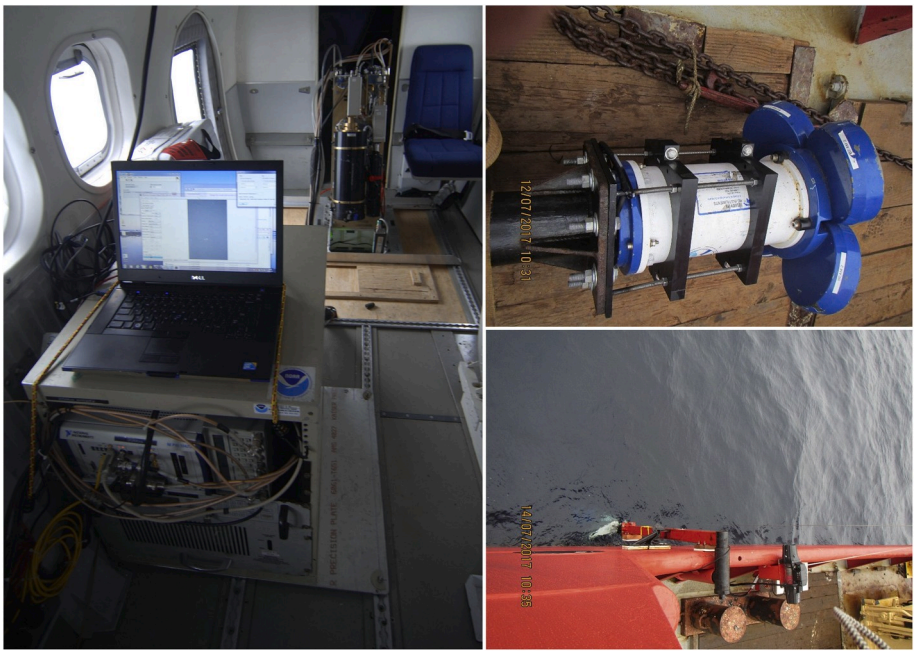

**Fig. 2.** Photos of lidar in aircraft (left) showing the optics package in center of the cabin at the rear and the electronics rack and laptop computer in the foreground. On the right are the ADCP (top) and the installation on the side of the vessel (bottom).

depth was at the bottom of the surface mixed layer. Lidar flights came within 50 km of this mooring on three days, July 22, 26, and 28, 2017.

Water density was also measured by CTD cast from the USCGC *Healy* at 71.223°N, 164.262°W on July 29, 2017 and 72.473°N, 156.567°W on August 3, 2017. The first position was within 500 m of the Prawler position. Lidar flights came within 50 km of the second position on July 18, 27, and 29, 2017.

We also have CTD casts from 10 positions across Barrow Canyon (Fig. 2) measured on July 21 and 22, 2017 from the CCGS *Sir Wilfrid Laurier*. In addition to calculating mixed layer depths for these casts, we calculated the positions of various water masses across the canyon according to the classifications of Gong and Pickard (2015).

During the same period, a 150 kHz Acoustic Doppler Current Profiler (ADCP, Fig. 2) was operated from the ship, which made four passes along the CTD line in Fig. 2. To see if the ADCP measured turbulence over a range of wavelengths similar to the lidar, we calculated the power spectral density of the acoustic backscatter intensity at three depths – 11, 19, and 39 m. Because the scattering mechanisms are different, we were not interested in comparing the magnitude of mixing between lidar and ADCP. As with the lidar, a single sample was used from each acoustic ping to create the data series for each spectrum. The 8° two-way beam width of the ADCP implies that spatial wavelengths greater than 650, 380, and 180 $km^{-1}$ cannot be measured at the three depths used. These wavelengths were greater than the noise limit for all cases.

Large-scale winds were obtained from the National Centers for Environmental Prediction (NCEP) North American Regional Reanalysis (Mesinger et al., 2006). These were averaged over the period of the flights (July 15–31) for each year. Only values over water and between −170° and −168° longitude were used in the analysis. This roughly corresponds to the longitudinal extent of the Bering Strait.

The Bakun upwelling index (Bakun, 1973, 1990) was calculated using the hourly wind speed and direction at the Wiley Post-Will Rogers Memorial Airport in Utqiaġvik, Alaska. For this calculation, a value of 34° from the east-west direction was used for the orientation of the coastline. This is the angle of a line from Point Barrow to Point Hope along the northwest coast of Alaska.

## 3. Results

An example of layers in broken ice (Fig. 4) shows two layers – one at

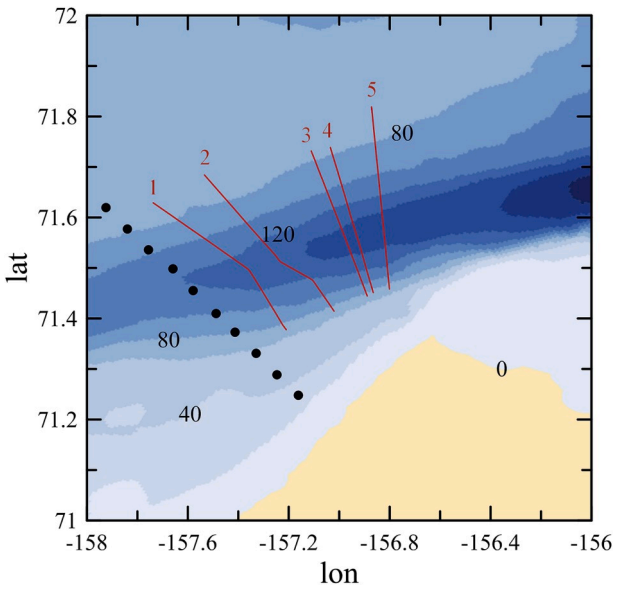


**Fig. 3.** Map of region near Point Barrow, Alaska, with bathymetry denoted by color scale at depth intervals of 20 m. Flight segments from 2017 are denoted by red lines and numbered from west to east. Ship stations are denoted by black circles. (For interpretation of the references to color in this figure legend, the reader is referred to the Web version of this article.)

a depth of about 20 m and another at a depth of about 30 m. The lidar does not penetrate through ice, but layers are visible wherever the lidar is able to penetrate between ice floes; they appear as vertical white bands in the image. They can even be seen in the first km of the image, where the ice fraction is 86%. Note also that the penetration into the water does not depend on ice fraction. This figure illustrates the ability of airborne lidar to measure subsurface plankton layers with high horizontal and vertical resolution, even in broken ice.

The ice conditions were very different in the latter half of July in the two years (Fig. 1), and this difference shows up in survey conditions (Fig. 5a). The surveys in 2017 were much more likely to be over open water (ice fraction $< 0.1$), less likely to be over broken ice, and slightly more likely to be over complete ice cover (ice fraction $> 0.9$). Qualitatively, we noticed that the transition from open water to tightly packed floes occurred much more rapidly in the 2017 flights. This figure was included to acknowledge that sampling bias might be a factor in our results. Clearly, the smaller sample sizes in broken ice in 2017 produce larger error bars in the probability of detecting a layer (Fig. 5b).

The probability of encountering a subsurface plankton layer in 2017 was greater than in 2014, except in open water (Fig. 5b). For 2014, the

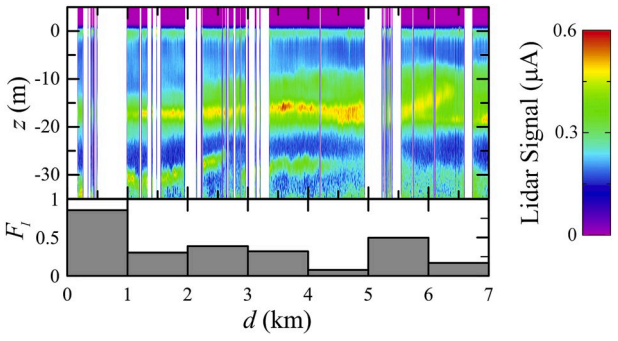


**Fig. 4.** Top is lidar signal current as a function of depth, $z$, and position along the flight track, $d$, for a 7 km segment of data. Color scale at the right shows signal current levels. Vertical white regions denote regions of ice. Bottom is a bar chart of the corresponding ice fraction, $F_I$, in 1 km segments.

layer probability decreased with increasing ice fraction, with a coefficient of determination of $R^2 = 0.52$ ($p = 0.02$). Without the open water value, the correlation was much higher, with $R^2 = 0.90$ ($p < 10^{-4}$). For 2017, the correlation was much higher when all values were used, with $R^2 = 0.83$ ($p < 0.001$). Without the open water point, the correlation was slightly less than in 2014, with $R^2 = 0.86$ ($p < 0.001$).

For both years, an exponential model for the relationship between ice fraction and the probability of encountering a subsurface plankton layer explained most of the variance in the latter. Within the region of broken ice (fraction $> 0.1$), the exponential model explained 90% of the observed variability in 2014 and 86% of the variability in 2017. The rate of decay for the two years was very similar, although the overall levels were different. In general, $P_L = A \exp(-2.32 F_I)$, where $P_L$ is the probability of a layer and $F_I$ is the ice fraction. The difference in the coefficient of $F_I$ between the two years was about 5% of the reported mean value. The constant, $A$, was 0.18 in 2014 and twice as large (0.37) in 2017.

The mean characteristics of the layers for both years are listed in Table 1, including a column for layers south of 72° N. This area, where most of the 2014 surveys took place (Fig. 1), was almost entirely open water in 2017. The most notable feature is the difference in layer strength; the average and median strength of the layers was much weaker in 2017 than 2014. For both years, layers in open water were stronger than those in broken ice. Open water layers south of 72° were stronger than the overall average, but still only about half as strong as open water layers in 2014. Average layer depths were about the same for both years, with open water layers slightly deeper than those in broken ice. Layers in 2017 were thinner than those in 2014, with little difference between the thickness in open water and ice in either year.

The average depth of layers within 50 km of the Prawler was 27.0 m with a standard deviation of 8.8 m. The average depth of the mixed layer inferred from the Prawler data was 25.6 m with a standard deviation of 1.7 m. The difference in the average depths, 1.4 m, is about 13% of the combined standard deviations.

The mixed layer depths inferred from the two ship-based casts were 23 m and 29 m. Note that the first cast was within 500 m of the Prawler, so the same lidar data were compared with the Prawler and with the first ship cast. The average (±standard deviation) depth of the plankton layers in these data was 27.0 ± 8.8 m. For the other cast, the average layer depth was 16.2 ± 8.1 m, which is well above the mixed layer depth of 29 m inferred from the CTD cast. However, there was a second density gradient at about 14 m, which is much closer to the average layer depth. The Brunt-Väisälä frequency at this depth was 0.041 $s^{-1}$, which is of a similar magnitude to the peak value of 0.053 $s^{-1}$ at 29 m.

The average mixed layer depth across the Barrow Canyon casts was 11.9 m, with a standard deviation of 4.0 m. Stratification was weak, with the mean of the peak Brunt-Väisälä frequency only $5.4 \times 10^{-3}$ $s^{-1}$ and the standard deviation $3.1 \times 10^{-3}$ $s^{-1}$. The average depth of plankton layers across the five lidar transects of the canyon was 17.8 m, with a standard deviation of 7.4 m. The layers were also weak, with a mean and standard deviation of 1.98 ± 1.06 times the background scattering level. Both depth and strength of layers increased as the distance from the mouth of the canyon increased.

Using the CTD data, three water masses were found across Barrow Canyon (Fig. 6). Alaskan Coastal Water (ACW), warm (>3 °C) and moderately salty (30–32.5 psu), covered the surface and extended to the bottom on the south side of the canyon. Winter Water (WW), cold (<−1.6 °C) and salty (31.5–33.6 psu), was below 30 m on the north side of the canyon. Chukchi Summer Water (CSW), with intermediate temperature (-1 – 3 °C) and salinity (30–32.8), was found primarily in a layer around 25 m on the north side of the canyon and to the bottom in the deepest part of the canyon.

The power spectral density of the fluctuations in lidar signal were very close to a power law with exponent of −5/3 for all five passes over Barrow Canyon and for both depths. A typical spectrum (Fig. 7) shows a power-law shape until the lidar noise limit is reached at high spatial wavelengths. For this case, the fit was performed up to a wavelength of

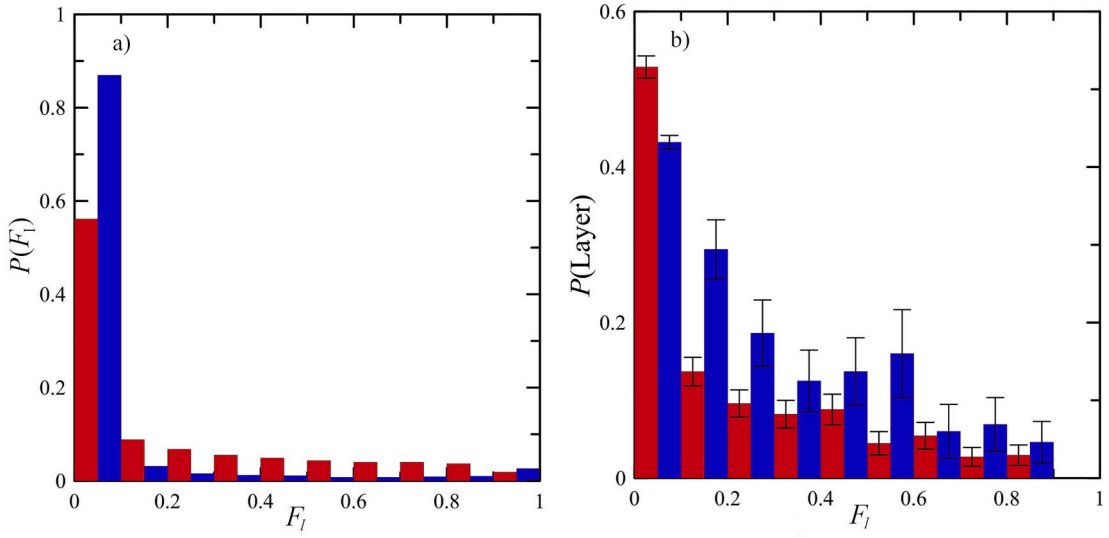


**Fig. 5.** a) Probability of encountering a given fractional ice cover, $F_I$, in increments of 0.1 for 2014 (red) and 2017 (blue). **b)** Probability of encountering a subsurface plankton layer as a function of ice fraction for 2014 (red) and 2017 (blue). Error bars represent ±1 standard deviation of the values. (For interpretation of the references to color in this figure legend, the reader is referred to the Web version of this article.)

**Table 1**
Strength (average, standard deviation, and median in next line), average and standard deviation depth, and average and standard deviation thickness for layers identified in 2014 and 2017. Columns present values for open water and broken ice for each year, and open water south of 72°N for 2017 (In, 2014, all open water was south of 72°N).

| 2014 | Open Water | Ice >0.1 | 2017: | Open Water | Ice >0.1 | South of 72° |
|---|---|---|---|---|---|---|
| Strength | 27.0 ± 44.7 | 8.9 ± 14.0 | | 10.7 ± 48.9 | 4.1 ± 5.6 | 13.4 ± 55.3 |
| Median | 12 | 5.1 | | 2.6 | 2.2 | 3.0 |
| Depth (m) | 19.6 ± 6.0 | 15.6 ± 6.2 | | 18.5 ± 8.1 | 15.5 ± 7.0 | 20.1 ± 8.2 |
| Thickness (m) | 3.8 ± 1.5 | 3.4 ± 2.0 | | 2.4 ± 1.6 | 2.8 ± 1.7 | 2.3 ± 1.6 |

40 km$^{-1}$, and the exponent of −1.70 is within 2% of the expected value.

The characteristics of power spectral density for the five passes and two depths are presented in Table 2, along with the Bakun upwelling index estimated from Utqiaġvik winds. The correlation between upwelling and turbulence level was 0.91 (P = 0.03) at 10 m and 0.88 (P = 0.05) at 20 m. During periods of downwelling (negative index), turbulence levels were all below $10^{-17}$, and the differences between the

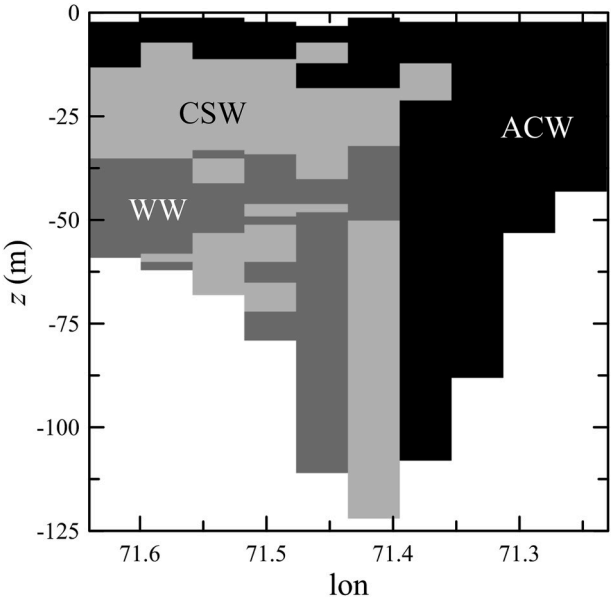


**Fig. 6.** Distribution of Gong-Pickard water masses across Barrow Canyon. Colors represent Alaskan Coastal Water (ACW, black), Winter Water (WW, dark gray), and Chukchi Summer Water (CSW, light gray).

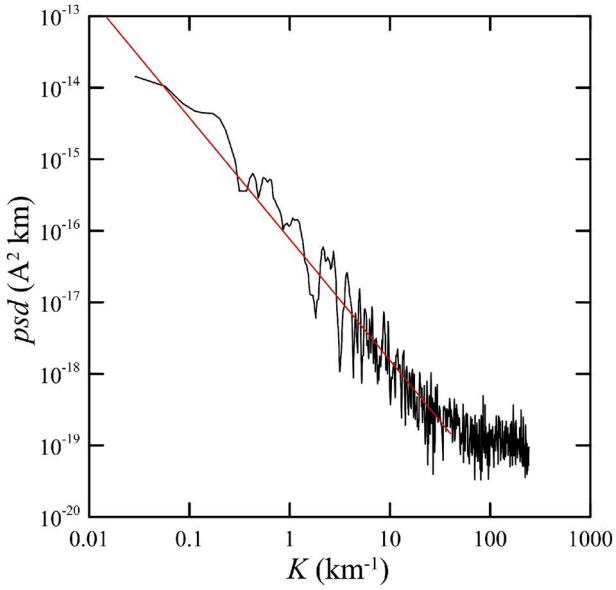


**Fig. 7.** Power spectral density, *psd*, as a function of spatial wavelength, *K*, for lidar data collected at 10 m depth on July 28, 2017. Red line is the result of a linear regression from the first value to 40 km$^{-1}$. (For interpretation of the references to color in this figure legend, the reader is referred to the Web version of this article.)

**Table 2**
Line number (from west to east in Fig. 2), date (July 2017) of the measurement, Bakun upwelling index ($m^3\ s^{-1}$ per 100 m of coastline), turbulence level, $T$ ($A^2$ km) at 10 m and 20 m depths, and the percent difference between them.

| Line (W to E) | Date | Upwelling | $T_{10}$ | $T_{20}$ | Difference (%) |
|---|---|---|---|---|---|
| 1 | 21 | −177 | $7.96 \times 10^{-18}$ | $7.45 \times 10^{-18}$ | 6 |
| 2 | 28 | 58 | $1.12 \times 10^{-16}$ | $4.50 \times 10^{-17}$ | 60 |
| 3 | 29 | −509 | $3.43 \times 10^{-18}$ | $3.08 \times 10^{-18}$ | 10 |
| 4 | 31 | −310 | $2.95 \times 10^{-18}$ | $3.11 \times 10^{-18}$ | 5 |
| 5 | 18 | 64 | $4.09 \times 10^{-17}$ | $1.31 \times 10^{-17}$ | 68 |

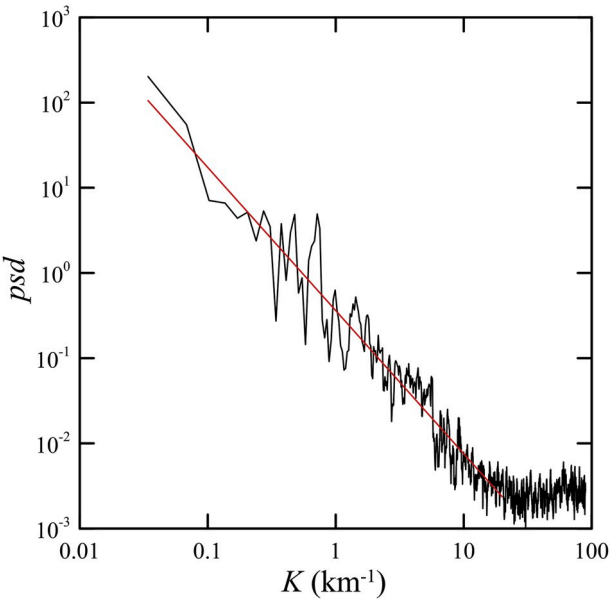


**Fig. 8.** Power spectral density, *psd*, as a function of spatial wavelength, *K*, for acoustic data collected at 39 m depth on July 22, 2017. Red line is the result of a linear regression from the first value to 20 $km^{-1}$. (For interpretation of the references to color in this figure legend, the reader is referred to the Web version of this article.)

levels at the two depths were 10% or less of the value at 10 m. During upwelling conditions, turbulence levels were higher ($>10^{-17}$) and the difference was 60% or greater.

The acoustic spectra (Fig. 8) are very similar to the lidar spectra; a power law with slope near −5/3 and a nearly white noise floor at high wavelengths. While the spatial scales are similar to those measured by the lidar, the magnitudes are very different; this is simply because we used different measures of signal level for the two instruments, and they have different units. For the case presented, the slope of −1.68 was within 1% of the expected value out to a wavelength of 20 $km^{-1}$. These data were collected over too short a time period to investigate the effects of upwelling on turbulence level, but we did find a significant increase of turbulence with depth ($R = 0.76$, $P = 0.005$) over the three depths investigated.

## 4. Discussion

Much of the difference in ice cover can be explained by a difference in winds between 2014 and 2017. On the northern Chukchi Shelf, the mean winds (NCEP reanalysis) in June and July of 2014 were toward the southwest at ~0.7 m $s^{-1}$. In sharp contrast, in June and July of 2017 the winds were toward the west-northwest at > 2 m $s^{-1}$. Thus, during the months of strong melt-back on the northern Chukchi Shelf, we would expect the sea ice to be pushed farther north in 2017 and pushed weakly southward in 2014. The transport of sea ice in 2014 southward is limited by relatively warm surface temperatures and by relatively weak northward transport through Barrow Canyon (Stabeno et al., 2018). We would also expect individual floes to be pushed together by the winds in 2017, resulting in smaller areas with partial ice cover and more areas with almost complete ice cover. These features are consistent with the differences seen in Fig. 3. This is also consistent with visual observations of areas of complete ice cover from the aircraft; in 2014, these areas appeared to be mostly solid ice, while in 2017, they appeared to be mostly closely packed ice floes. The change in ice conditions seems less likely to be related to global changes. For the northern hemisphere, the average ice extent over the last half of July only decreased by 1.5% from 2014 to 2017, while the corresponding decrease in the Chukchi Sea was 20% (Fetterer et al., 2010).

It is not clear why so much of the variability would be explained by ice fraction. One possibility is that the stratification increases as the ice melts, so the density gradients that support thin plankton layers increase as the ice fraction decreases.

The biggest difference in plankton layer properties between the two years was the layer strength in both open water and in broken ice. Because the layer strength is defined as the ratio of the layer signal to the background, this difference could be because the concentrations of phytoplankton within the layers were lower in 2017, the background concentrations were greater, or some combination of the two. To answer this question, we used chlorophyll concentration composites for the month of July in each year from the Visible and Infrared Imager/Radiometer Suite (VIIRS). We assumed that this average of surface chlorophyll concentration would be correlated with the average of the background lidar scattering parameter obtained from the perturbation inversion of the lidar depth profiles. For pixels (at 4-km resolution) in US Arctic waters with data for both years, the average increase in surface chlorophyll concentration from 2014 to 2017 was 72%. The mean layer strength in open water south of 72°N was 50% of the strength in open water in 2014, all of which was south of 72°. This would suggest that much of the difference was caused by an increase in background levels, coupled with a smaller decrease in phytoplankton concentrations within the layers.

The average depths of layers in open water and in broken ice were nearly the same for both years, and, in both cases, slightly deeper in open water (Table 1). In 2017, the depths agreed with available measurements of pycnocline depth to within the variability of the measurements. In general, layer depths were slightly greater than pycnocline depth, however. Our depths are also consistent with *in situ* measurements of layer depths that range from 15 to 25 m (Brown et al., 2015; Coupel et al., 2011; Hill and Cota, 2005; Martini et al., 2016).

The average layer thickness was slightly less in 2017 than in 2014. This difference may also be at least partially explained by the difference in winds. A model of layer thickness based on current shear predicts a minimum thickness of (Birch et al., 2008)

$$t = 2.4\alpha^{-1/3}\kappa_\nu^{1/3}L_0^{1/3}, \quad (2)$$

where $\alpha$ is vertical current shear, $\kappa_\nu$ is the vertical diffusivity of plankton, and $L_0$ is the initial horizontal extent of the plankton patch before thinning by shear. In this simple model, the initial vertical extent does not matter. The factor of 2.4 is the result of converting from a Gaussian radius to full width at half maximum. Using typical parameters from Birch et al. (2008), the predicted minimum thickness is approximately

what we observed in 2017. The thicker layers in 2014 could be explained by a current shear of about one fourth of the 2017 values. One might expect that the weaker winds in 2014 would produce lower surface drift currents and less shear. However, current shear measurements from ADCP moorings east of Barrow Canyon (31 km from shore in 45 m of water at 71.2°N, 158.0°W) were generally higher during the last half of July in 2014 than in the same period of 2017. It is not clear whether the current shear measured at this location is not representative of the larger survey area or if some other mechanism is controlling layer thickness.

The difference between the ice conditions is mainly due to interannual variability, but our results suggest what may happen in the future as the July ice edge moves farther north. The prevalence of subsurface plankton layers might increase, while their intensity relative to the background concentration might decrease. The exponential decrease in layer prevalence should continue with the same dependence on ice cover. Similarly, the depth of layers would not be expected to change significantly. From a biological perspective, the increased prevalence of subsurface plankton layers could lead to increases in both primary and secondary productivity (Durham and Stocker, 2011). The higher density of phytoplankton in the layer, relative to the nutrient-depleted surface water, produces faster recycling of nutrients and higher grazing rates by zooplankton and pelagic fish. Conceivably, this could support a northward expansion of some pelagic fish species.

Except at the very limit of depth penetration, the lidar measurements in Barrow Canyon were made in either Alaskan Coastal Water or Chukchi Summer Water. This is consistent with previous measurements of water masses in Barrow Canyon in summer, although some authors used different identifiers and different parameter ranges (Coachman and Barnes, 1961; Crawford et al., 2012; Weingartner et al., 1998). Therefore, it is mixing of these two water masses that provides the turbulence observed by the lidar and the ADCP at the two shallower depths. At 40 m, the ADCP is also influenced by Winter Water (Fig. 6).

Turbulent mixing of phytoplankton in Barrow Canyon is enhanced by wind-driven upwelling. Another hypothesis, that tidal currents might be a factor, was not considered, because tidal currents are very small in Barrow Canyon (Itoh et al., 2013; Mountain et al., 1976). We also observed that measured turbulence levels were higher at 10 m than at 20 m during upwelling, but nearly the same during downwelling conditions. This result is probably related to greater vertical gradients during upwelling conditions. For our data, the average lidar signal across the canyon was 19% higher at 10 m than at 20 m during upwelling, but 2.6% lower during downwelling.

While the lidar return is dominated by phytoplankton (Churnside and Thorne, 2005), the ADCP return is mostly from zooplankton (Flagg and Smith, 1989; Ressler, 2002). This might explain why the turbulence levels observed by the ADCP increase with increasing depth. The spectrum of zooplankton can also be affected by individuals swimming, but the observed −5/3 power law is strong evidence that this has a minimal effect. Zooplankton can be detected by lidar (Churnside and Thorne, 2005), but the required processing reduces the signal to noise ratio, and it was not possible to obtain clear spectra of the zooplankton return.

For a passive scalar quantity, $\theta$, the turbulence level defined above is given by

$$T = C_\theta \langle \varepsilon \rangle^{-1/3} \langle \chi \rangle, \tag{3}$$

where $C_\theta$ is the Obukhov-Corrsin constant (~0.4), $\langle \varepsilon \rangle$ is the mean energy dissipation rate, and the dissipation rate of the variance of the scalar is given by

$$\langle \chi \rangle = 2\kappa_\nu \langle |\nabla \theta|^2 \rangle, \tag{4}$$

where $\kappa_\nu$ is the scalar diffusivity and $\nabla\theta$ is the scalar gradient (Sreenivasan, 1996). This suggests that the difference in the vertical distribution of turbulence level observed by the lidar and the ADCP is because of differences in the vertical distribution of gradients of phytoplankton and zooplankton.

## 5. Conclusions

Ice conditions were very different in the study area in July of 2014 and 2017, but the characteristics of subsurface plankton layers and their dependence on ice cover were similar for the two years. In both years, the prevalence of subsurface plankton layers exponentially decreased with increasing ice cover. The average depths were similar for both years, with layers in open water deeper than those in the pack ice. The depths of subsurface plankton layers were consistent with the mixed layer depth in areas where *in situ* density profiles were available. A noticeable difference in layer strength relative to the background water was likely caused by higher background phytoplankton concentrations in 2017. Differences in layer thickness were observed, which could be the result of higher current shears in 2017.

Turbulent mixing of phytoplankton and zooplankton in Barrow Canyon was inferred from the power spectral density of lidar and acoustic scattering. Lidar measurements suggested that the level of turbulence and its vertical distribution were affected by local upwelling winds. The vertical distribution of acoustic scattering was different from that of the lidar, which we interpret as different vertical distributions of phytoplankton and zooplankton gradients.

## Declaration of competing interest

The authors declare that they have no known competing financial interests or personal relationships that could have appeared to influence the work reported in this paper.

## CRediT authorship contribution statement

**James H. Churnside:** Conceptualization, Methodology, Investigation, Writing - original draft. **Richard D. Marchbanks:** Investigation, Software. **Svein Vagle:** Investigation, Writing - review & editing. **Shaun W. Bell:** Software, Data curation, Writing - review & editing. **Phyllis J. Stabeno:** Investigation, Writing - review & editing.

## Acknowledgments

We would like to acknowledge our pilots, Shanae Coker and Frank Centinello III, mechanic, Robert Miletic, and the captain and crew of CCGS Sir Wilfrid Laurier. Satellite ice extent were obtained from the US National Ice Center (https://www.natice.noaa.gov/). Large-scale wind data were obtained from the NOAA Earth System Research Laboratory Physical Sciences Division (https://www.esrl.noaa.gov/psd/cgi-bin/data/narr/plothour.pl). Hourly wind speed and direction at the Wiley Post-Will Rogers Memorial Airport were obtained from the Weather Underground archive (https://www.wunderground.com/history/). Satellite chlorophyll data were obtained from the NASA Goddard Space Flight Center, Ocean Ecology Laboratory, Ocean Biology Processing Group. Visible and Infrared Imager/Radiometer Suite (VIIRS) Ocean Color Data; 2018 Reprocessing. NASA OB.DAAC, Greenbelt, MD, USA. https://doi.org/10.5067/NPP/VIIRS/L2/OC/2018, accessed on 08/22/2018. The authors have no conflict of interest. Lidar data from this study are available at https://data.nodc.noaa.gov/cgi-bin/iso?id=gov.noaa.nodc:0187514. This publication is contribution #4896 from the Pacific Marine Environmental Laboratory. This work was partially supported by the United States National Aeronautics and Space Administration grant NNH16AD24I.

## Appendix A. Supplementary data

Supplementary data to this article can be found online at https://doi.org/10.1016/j.dsr2.2020.104742.

## References


Ardyna, M., Babin, M., Gosselin, M., Devred, E., Bélanger, S., Matsuoka, A., Tremblay, J.É., 2013. Parameterization of vertical chlorophyll a in the Arctic Ocean: impact of the subsurface chlorophyll maximum on regional, seasonal, and annual primary production estimates. Biogeosciences 10, 4383–4404. https://doi.org/10.5194/bg-10-4383-2013.

Arrigo, K.R., van Dijken, G.L., 2015. Continued increases in Arctic Ocean primary production. Prog. Oceanogr. 136, 60–70. https://doi.org/10.1016/j.pocean.2015.05.002.

Arrigo, K.R., van Dijken, G., Pabi, S., 2008. Impact of a shrinking Arctic ice cover on marine primary production. Geophys. Res. Lett. 35, L19603. https://doi.org/10.1029/2008gl035028.

Arrigo, K.R., Matrai, P.A., van Dijken, G.L., 2011. Primary productivity in the Arctic Ocean: impacts of complex optical properties and subsurface chlorophyll maxima on large-scale estimates. J. Geophys. Res. Oceans 116, C11022. https://doi.org/10.1029/2011jc007273.

Arrigo, K.R., et al., 2014. Phytoplankton blooms beneath the sea ice in the Chukchi sea. Deep Sea Res. II 105, 1–16. https://doi.org/10.1016/j.dsr2.2014.03.018.

Bakun, A., 1973. Coastal Upwelling Indices, West Coast of North America, 1946-71. NOAA Technical Report Rep. NMFS SSRF-693. U.S. Department of Commerce, Seattle, Washington.

Bakun, A., 1990. Global climate change and intensification of coastal ocean upwelling. Science 247, 198.

Behrenfeld, M.J., et al., 2017. Annual boom–bust cycles of polar phytoplankton biomass revealed by space-based lidar. Nat. Geosci. 10, 118. https://doi.org/10.1038/ngeo2861. https://www.nature.com/articles/ngeo2861#supplementary-information.

Birch, D.A., Young, W., Franks, P., 2008. Thin layers of plankton: formation by shear and death by diffusion. Deep Sea Res. I 55, 277–295. https://doi.org/10.1016/j.dsr.2007.11.009.

Bourgain, P., Gascard, J.C., 2011. The Arctic Ocean halocline and its interannual variability from 1997 to 2008. Deep Sea Res. I 58, 745–756. https://doi.org/10.1016/j.dsr.2011.05.001.

Brown, Z.W., Lowry, K.E., Palmer, M.A., van Dijken, G.L., Mills, M.M., Pickart, R.S., Arrigo, K.R., 2015. Characterizing the subsurface chlorophyll a maximum in the Chukchi Sea and Canada basin. Deep Sea Res. II. https://doi.org/10.1016/j.dsr2.2015.02.010.

Churnside, J.H., 2014. Review of profiling oceanographic lidar. Opt. Eng. 53 https://doi.org/10.1117/1.oe.53.5.051405, 051405-051405.

Churnside, J.H., Thorne, R.E., 2005. Comparison of airborne lidar measurements with 420 kHz echo-sounder measurements of zooplankton. Appl. Optic. 44, 5504–5511. https://doi.org/10.1364/AO.44.005504.

Churnside, J.H., Ostrovsky, L.A., 2005. Lidar observation of a strongly nonlinear internal wave train in the Gulf of Alaska. Int. J. Rem. Sens. 26, 167–177. https://doi.org/10.1080/01431160410001735076.

Churnside, J.H., Donaghay, P.L., 2009. Thin scattering layers observed by airborne lidar. ICES J. Mar. Sci. 66, 778–789. https://doi.org/10.1093/icesjms/fsp029.

Churnside, J.H., Marchbanks, R.D., 2015. Sub-surface plankton layers in the Arctic Ocean. Geophys. Res. Lett. 42, 4896–4902. https://doi.org/10.1002/2015GL064503.

Churnside, J.H., Marchbanks, R.D., 2017. Inversion of oceanographic profiling lidars by a perturbation to a linear regression. Appl. Optic. 56, 5228–5233. https://doi.org/10.1364/AO.56.005228.

Churnside, J.H., Marchbanks, R.D., Lee, J.H., Shaw, J.A., Weidemann, A., Donaghay, P.L., 2012. Airborne lidar detection and characterization of internal waves in a shallow fjord. J. Appl. Remote Sens. 6 https://doi.org/10.1117/1.jrs.6.063611, 063611-063615.

Coachman, L.K., Barnes, C.A., 1961. The contribution of Bering sea water to the Arctic Ocean. Arctic 14, 147–161.

Comiso, J.C., 2011. Large decadal decline of the Arctic multiyear ice cover. J. Clim. 25, 1176–1193. https://doi.org/10.1175/jcli-d-11-00113.1.

Cota, G., Pomeroy, L., Harrison, W., Jones, E., Peters, F., Sheldon, W.J., Weingartner, T., 1996. Nutrients, primary production and microbial heterotrophy in the southeastern Chukchi Sea: Arctic summer nutrient depletion and heterotrophy. Mar. Ecol. Prog. Ser. 135, 247–258. https://doi.org/10.3354/meps135247.

Coupel, P., Jin, H.Y., Ruiz-Pino, D., Chen, J.F., Lee, S.H., Li, H.L., Rafizadeh, M., Garçon, V., Gascard, J.C., 2011. Phytoplankton distribution in the Western Arctic Ocean during a summer of exceptional ice retreat. Biogeosci. Discuss. 8, 6919–6970. https://doi.org/10.5194/bgd-8-6919-2011.

Crawford, R.E., Vagle, S., Carmack, E.C., 2012. Water mass and bathymetric characteristics of polar cod habitat along the continental shelf and slope of the Beaufort and Chukchi seas. Polar Biol. 35, 179–190. https://doi.org/10.1007/s00300-011-1051-9.

Durham, W.M., Stocker, R., 2011. Thin phytoplankton layers: characteristics, mechanisms, and consequences. Annu. Rev. Mar. Sci. 4, 177–207. https://doi.org/10.1146/annurev-marine-120710-100957.

Fetterer, F., Savoie, M., Helfrich, S., Clement-Colon, P., 2010. Multisensor analyzed sea ice extent - northern hemisphere (MASIE-NH), Version 1. In: Daily Ice Extent. National Ice Center and National Snow and Ice Data Center, Boulder, Colorado, USA. https://doi.org/10.7265/N5GT5K3K.

Flagg, C.N., Smith, S.L., 1989. On the use of the acoustic Doppler current profiler to measure zooplankton abundance. Deep Sea Res. A. 36, 455–474. https://doi.org/10.1016/0198-0149(89)90047-2.

Goldin, Y.A., Vasilev, A.N., Lisovskiy, S.S., Chernook, V.I., 2007. Results of Barents Sea airborne lidar survey. In: Proc. 6615, Current Research on Remote Sensing, Laser Probing, and Imagery in Natural Waters. SPIE, Bellingham, p. 66150E. https://doi.org/10.1117/12.740456.

Gong, D., Pickart, R.S., 2015. Summertime circulation in the eastern Chukchi Sea. Deep Sea Res. II 118, 18–31. https://doi.org/10.1016/j.dsr2.2015.02.006.

Grebmeier, J.M., Moore, S.E., Overland, J.E., Frey, K.E., Gradinger, R., 2010. Biological response to recent Pacific Arctic sea ice retreats. Eos, Trans. Am. Geophys. Union 91, 161–162. https://doi.org/10.1029/2010EO180001.

Hegseth, E.N., 1998. Primary production of the northern Barents Sea. Polar Res. 17, 113–123. https://doi.org/10.1111/j.1751-8369.1998.tb00266.x.

Hill, V., Cota, G., 2005. Spatial patterns of primary production on the shelf, slope and basin of the Western Arctic in 2002. Deep Sea Res. II 52, 3344–3354. https://doi.org/10.1016/j.dsr2.2005.10.001.

Hill, V., Cota, G., Stockwell, D., 2005. Spring and summer phytoplankton communities in the Chukchi and eastern Beaufort seas. Deep Sea Res. II 52, 3369–3385. https://doi.org/10.1016/j.dsr2.2005.10.010.

Hill, V.J., Zimmerman, R.C., 2010. Estimates of primary production by remote sensing in the Arctic Ocean: assessment of accuracy with passive and active sensors. Deep Sea Res. I 57, 1243–1254. https://doi.org/10.1016/j.dsr.2010.06.011.

Itoh, M., Nishino, S., Kawaguchi, Y., Kikuchi, T., 2013. Barrow Canyon volume, heat, and freshwater fluxes revealed by long-term mooring observations between 2000 and 2008. J. Geophys. Res. Oceans 118, 4363–4379. https://doi.org/10.1002/jgrc.20290.

Jacox, M.G., Edwards, C.A., Kahru, M., Rudnick, D.L., Kudela, R.M., 2015. The potential for improving remote primary productivity estimates through subsurface chlorophyll and irradiance measurement. Deep Sea Res. II 112, 107–116. https://doi.org/10.1016/j.dsr2.2013.12.008.

Jakobsson, M., et al., 2012. The international bathymetric chart of the Arctic Ocean (IBCAO) Version 3.0. Geophys. Res. Lett. 39, L12609 https://doi.org/10.1029/2012GL052219.

Kitchen, J.C., Zaneveld, J.R.V., 1990. On the noncorrelation of the vertical structure of light scattering and chlorophyll α in case I waters, 95, pp. 20237–20246. https://doi.org/10.1029/JC095iC11p20237.

Kwok, R., Rothrock, D.A., 2009. Decline in Arctic sea ice thickness from submarine and ICESat records: 1958–2008. Geophys. Res. Lett. 36, L15501. https://doi.org/10.1029/2009gl039035.

Lee, Y., et al., 2015. An assessment of phytoplankton primary productivity in the Arctic Ocean from satellite ocean color/in situ chlorophyll-a based models. J. Geophys. Res. Oceans 120, 6508–6541. https://doi.org/10.1002/2015jc011018.

Lu, X., Hu, Y., Liu, Z., Rodier, S., Vaughan, M., Lucker, P., Trepte, C., Pelon, J., 2017. Observations of Arctic snow and sea ice cover from CALIOP lidar measurements. Remote Sens. Environ. 194, 248–263. https://doi.org/10.1016/j.rse.2017.03.046.

Martin, J., Dumont, D., Tremblay, J.-É., 2013. Contribution of subsurface chlorophyll maxima to primary production in the coastal Beaufort Sea (Canadian Arctic): a model assessment. J. Geophys. Res. Oceans 118, 5873–5886. https://doi.org/10.1002/2013JC008843.

Martin, J., Tremblay, J., Gagnon, J., Tremblay, G., Lapoussi, A., Jose, C., Poulin, M., Gosselin, M., Gratton, Y., Michel, C., 2010. Prevalence, structure and properties of subsurface chlorophyll maxima in Canadian Arctic waters. Mar. Ecol. Prog. Ser. 412, 69–84. https://doi.org/10.3354/meps08666.

Martini, K.I., Stabeno, P.J., Ladd, C., Winsor, P., Weingartner, T.J., Mordy, C.W., Eisner, L.B., 2016. Dependence of subsurface chlorophyll on seasonal water masses in the Chukchi Sea. J. Geophys. Res. Oceans 121, 1755–1770. https://doi.org/10.1002/2015JC011359.

Mesinger, F., et al., 2006. North American regional reanalysis. Bull. Am. Meteorol. Soc. 87, 343–360. https://doi.org/10.1175/bams-87-3-343.

Moore, S.E., Grebmeier, J.M., 2018. The distributed biological observatory: linking physics to biology in the Pacific Arctic region. Arctic 71, 1–7. https://doi.org/10.14460/arctic4606.

Mountain, D.G., Coachman, L.K., Aagaard, K., 1976. On the flow through Barrow canyon. J. Phys. Oceanogr. 6, 461–470. https://doi.org/10.1175/1520-0485(1976)006<0461:otftbc>2.0.co;2.

Naoya, K., Shin, S., Yoshihiko, O., Daiki, S., Yasushi, F., Daiki, N., 2018. Upwelling of macronutrients and dissolved inorganic carbon by a subglacial freshwater driven plume in Bowdoin Fjord, northwestern Greenland. J. Geophys. Res. Biogeosci. 123, 1666–1682. https://doi.org/10.1029/2017JG004248.

Osse, T.J., Meinig, C., Stalin, S., Milburn, H., 2015. The PRAWLER, a vertical profiler powered by wave energy. In: Paper Presented at OCEANS 2015. MTS/IEEE, Washington, 19-22 Oct. 2015.

Pithan, F., Mauritsen, T., 2014. Arctic amplification dominated by temperature feedbacks in contemporary climate models. Nat. Geosci. 7, 181–184. https://doi.org/10.1038/ngeo2071.

Ressler, P.H., 2002. Acoustic backscatter measurements with a 153kHz ADCP in the northeastern Gulf of Mexico: determination of dominant zooplankton and micronekton scatterers. Deep Sea Res. I 49, 2035–2051. https://doi.org/10.1016/S0967-0637(02)00117-6.

Retamal, L., Bonilla, S., Vincent, W.F., 2008. Optical gradients and phytoplankton production in the mackenzie river and the coastal Beaufort sea. Polar Biol. 31, 363–379. https://doi.org/10.1007/s00300-007-0365-0.

Ríos, F., Kilian, R., Mutschke, E., 2016. Chlorophyll-a thin layers in the Magellan fjord system: the role of the water column stratification. Continent. Shelf Res. 124, 1–12. https://doi.org/10.1016/j.csr.2016.04.011.

Serreze, M.C., Barry, R.G., 2011. Processes and impacts of Arctic amplification: a research synthesis. Global Planet. Change 77, 85–96. https://doi.org/10.1016/j.gloplacha.2011.03.004.

Shroyer, E.L., Benoit-Bird, K.J., Nash, J.D., Moum, J.N., 2014. Stratification and mixing regimes in biological thin layers over the Mid-Atlantic Bight. Limnol. Oceanogr. 59, 1349–1363. https://doi.org/10.4319/lo.2014.59.4.1349.

Spreen, G., Kwok, R., Menemenlis, D., 2011. Trends in Arctic sea ice drift and role of wind forcing: 1992–2009. Geophys. Res. Lett. 38, L19501. https://doi.org/10.1029/2011gl048970.

Sreenivasan, K.R., 1996. The passive scalar spectrum and the Obukhov-Corrsin constant. Phys. Fluids 8, 189–196. https://doi.org/10.1063/1.868826.

Stabeno, P., Kachel, N., Ladd, C., Woodgate, R., 2018. Flow patterns in the eastern Chukchi Sea: 2010–2015. J. Geophys. Res. Oceans 123, 1177–1195. https://doi.org/10.1002/2017JC013135.

Tabisola, H.M., Stabeno, P.J., Mordy, C.W., 2017. Using a biophysical mooring as a sentinel for ecosystem change: the story of M2. In: paper presented at OCEANS 2017, Anchorage, 18–21 Sept. 2017.

Taylor, P.C., Cai, M., Hu, A., Meehl, J., Washington, W., Zhang, G.J., 2013. A decomposition of feedback contributions to polar warming amplification. J. Clim. 26, 7023–7043. https://doi.org/10.1175/jcli-d-12-00696.1.

Vaughan, D.G., et al., 2013. Observations: cryosphere. In: Stocker, T.F., Qin, D., Plattner, G.-K., Tignor, M., Allen, S.K., Boschung, J., Nauels, A., Xia, Y., Bex, V., Midgley, P.M. (Eds.), Climate Change 2013: the Physical Science Basis. Contribution of Working Group I to the Fifth Assessment Report of the Intergovernmental Panel on Climate Change. Cambridge University Press, Cambridge, pp. 317–382.

Weingartner, T.J., Cavalieri, D.J., Aagaard, K., Sasaki, Y., 1998. Circulation, dense water formation, and outflow on the northeast Chukchi Shelf. J. Geophys. Res. Oceans 103, 7647–7661. https://doi.org/10.1029/98JC00374.

Weston, K., Fernand, L., Mills, D.K., Delahunty, R., Brown, J., 2005. Primary production in the deep chlorophyll maximum of the central North Sea. J. Plankton Res. 27, 909–922. https://doi.org/10.1093/plankt/fbi064.

Weston, K., Fernand, L., Mills, D.K., Delahunty, R., Brown, J., 2011. Primary production in the deep chlorophyll maximum of the central North Sea. J. Plankton Res. 33, 1627–1628. https://doi.org/10.1093/plankt/fbr067.